Selenate and Chromate Removal with Titanium Dioxide based Photocatalysts

by

Hangkun Jing

A Thesis Presented in Partial Fulfillment
of the Requirements for the Degree
Master of Science

Approved April 2018 by the
Graduate Supervisory Committee:

Candace Chan, Chair
Karl Sieradzki
Qinghua Wang

ARIZONA STATE UNIVERSITY

May 2018

ABSTRACT

As selenium and chromium are toxic even at low levels, it is very necessary to remove them from drinking water with proper ways. In this work, titanium dioxide based photocatalysts were mainly investigated in detail for their photoreduction ability towards selenate and chromate in aqueous environment. Firstly, photoreduction ability of layered double hydroxide (LDH) nanosheets with commercial TiO_2 particle hybrid materials was investigated towards selenate or chromate. The results showed that commercial LDH/TiO_2 (P90) composite, homemade LDH nanosheets/TiO_2 (P90) composite and also in situ LDH/TiO_2 (P25) composite all did not indicate significant improvement on photoreduction performance towards selenate or chromate. Secondly, TiO_2 nanosheets material was synthesized with TiS_2 as precursor via hydrothermal treatment. Morphology of TiO_2 nanosheets were characterized by SEM, AFM and TEM. Photodegradation of MB (methylene blue) with TiO_2 nanosheets was performed. In the future, first approach is to synthesize visible-light driven LDH photocatalyst NiFe-LDH nanosheets with TiO_2 nanosheets hybrid material for selenate removal. Second approach is to use anion intercalation/insertion via electrochemical process to remove anions in drinking water.

ACKNOWLEDGMENTS

I would like to thank my advisor Dr. Candace Chan for her help and guidance. She is very patient and devoted lots of energy to this work. Over the three years, I've learned a lot from her. She guides me on the experiment step by step. During this process, I learned how to analyze the data obtained and also what should do on the next step when problem occurs during the experiments. I felt like that no matter what field I am working on in the future, those ways of thinking and analyzing could be very helpful.

I would like to thank my committee members, Dr. Karl Sieradzki and Dr. Qinghua Wang for their suggestions and help.

I would also like to thank my group members, especially Man Li on her help during the experiments.

We greatly acknowledge the National Science Foundation Engineering Research Center (ERC) on Nanotechnology-Enabled Water Treatment (EEC-1449500) for the support. We also acknowledge the use of facilities within the LeRoy Eyring Center for Solid State Science and Goldwater Environmental Laboratory at Arizona State University.

At the end, I would like to thank my parents for their great love for me.

TABLE OF CONTENTS

Page

LIST OF TABLES

Table Page

LIST OF FIGURES

Figure Page

Figure Page

Figure Page

CHAPTER 1

INTRODUCTION

1. Introduction

Chromium is abundant in ground water and can naturally exist or produced by industrial activities, including metal finishing, dyeing, electroplating and steel fabrication, etc. [1, 2] Cr(VI) is mutagenic and carcinogenic and results in many health problems such as liver damage, pulmonary congestions, vomiting, even can cause cancer.[3-5] The limitation of chromium in drinking water is 0.1 ppm from U.S. Environmental Protection Agency.[6] So it is of great concern to eliminate Cr(VI) from our drinking water. The predominant form of the chromium states mainly depends on the pH of solution, concentration and redox potential, as indicated in Fig. 1.[7, 8] In aqueous environment, the most probable Cr(VI) states are $Cr_2O_7^{2-}$, CrO_4^{2-}, H_2CrO_4, and $HCrO_4^-$, which are all soluble anions and making it impossible to separate them by directly precipitating.[2, 7-9]

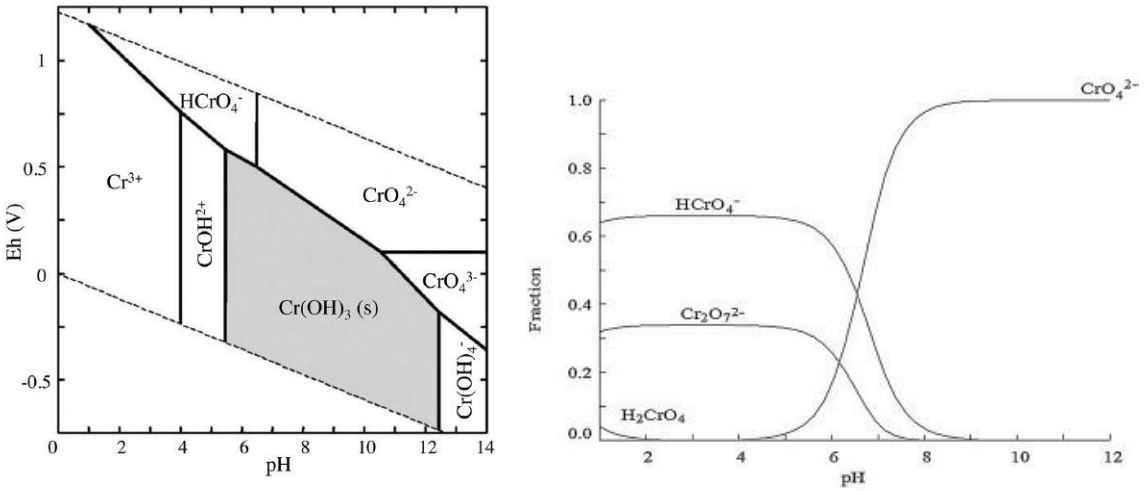

Fig.1 Eh-pH diagram for chromium species and Chromium speciation as a function of pH (Cr(VI) = 50 mg L^{-1})[7,10]

Selenium exists in many oxidation states, for example, selenide (Se^{2-}), elemental Se (Se^{0}), selenite (Se^{4+}), selenate (Se^{6+}), etc (Fig. 2). Selenite and selenate are soluble in water and therefore potentially toxic to animals and human beings. The reduced forms, most selenide (Se^{2-}) and elemental Se (Se^{0}) are insoluble therefore unavailable to aquatic environment. The presence of oxidized selenium in aquatic environment have been accelerated by agriculture irrigation and industrial wastewater, including electronics industry, glass industry, plastics, paints, enamels, inks, rubber, etc.[6] Epidemiological studies indicate that intake of low concentration of Se positively related with coronary heart disease, cardiovascular disease and cancer.[10] The maximum selenium concentration from U.S. Environmental Protection Agency is currently 50 ppb in drinking water. And the maximum allowable selenium level from the World Health Organization (WHO) and the EU in drinking water is 10 ppb.[11] Such stringent standards lead to a widespread exploration on the removal of selenium in drinking water.

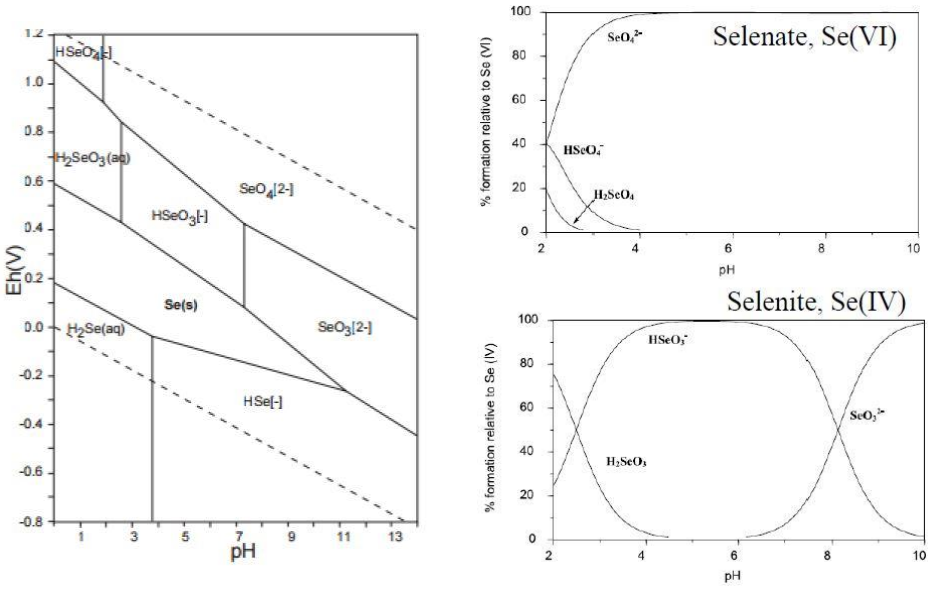

Fig. 2 Eh-pH diagram for selenium species and Selenium speciation as a function of pH[12]

In aqueous systems, selenate is harder to be removed from water compared to selenite, because selenate cannot be easily absorbed onto particles and selenite is easily immobilized.[13-16] The mechanism for adsorbance of selenate and selenite onto particles are quite different. For selenate, it prefer to bind through outer-sphere surface complexes and can only be weakly absorbed onto surface of metal oxides. For selenite, it prefers to bind through inner-sphere and can be absorbed strongly onto surface of metal oxides.[17-20] Sulfate has similar structure and physicochemical properties compared to selenate.[21] So when the sulfate is in high concentration in water, it can compete with selenate, which makes it hard to remove selenate.

Chromium (III) is a natural element which exists in soil, rocks, animals, plants, volcanic dust and gases. Trivalent chromium (Cr(III)) is another form of chromium in aqueous systems, which is 100-1000 times much less toxic than Cr(VI). It can also serve as a trace nutrient which enables living organisms to function properly. [2] Besides, from the Eh-pH diagram(Fig.1), it is indicated that at neutral pH Cr(III) exists in the form of insoluble $Cr(OH)_3$.[2, 7, 8] Therefore, to remove the toxic Cr(VI), except for adsorption, another commonly used method is to convert it to less toxic Cr(III) which can readily be precipitated out in the form of insoluble $Cr(OH)_3$.[22] Consequently, effective reduction of Cr(VI) to Cr(III) with innovative technologies has become a key procedure.

There are various technologies for the reduction of Cr(VI) to Cr(III). One of the chemical reduction treatments is using SO_2 gas or $NaHSO_3$ in acid solution as reducing agents. Both agents can form H_2SO_3 to reduce Cr(VI) and precipitate the chromium. However, the sludge produced during the whole reduction process is of large amount, which results in a big problem to manage, transport and final disposal. [7, 8] Another

traditional way to chemically reduce Cr(VI) is using iron(II) chloride and iron(II) sulfate as agents under acidic conditions, followed by precipitation with alkali. The disadvantages are that the considerable sludge produced, for instance, ferric hydroxide remains a big issue and also the requirement for a continuous supply of the reducing agents.[7, 8, 23]. An environmental compatible method to remove chromium from water is electrochemical technology, mainly since that electron is a "clean reagent". Electrocoagulation is one simple and efficient way to remove Cr(VI). Electrocoagulation is the electrochemical production of destabilization agents which can neutralize electric charge of the pollutants. One shortage of this method is that the sacrificial anode needs to be replaced periodically since it will be consumed gradually during the electrocoagulation reaction. Another electrochemical technology is electrochemical reduction using non-sacrificial anode. Carbon based electrodes, for instance, graphite and carbon felt, and also gold electrodes, conducting polymers are novel cathode materials which is very efficient for electrochemical Cr(VI) reduction. However, as compared to the electrocoagulation methods, it may needs relatively more treatment time and further separation/purification of Cr(III) products.

The removal of selenium mainly includes physical, chemical and biological methods. The physical methods mainly involve adsorption, ion-exchange and membrane processing. Physical removal is not an effective method for selenium removal compared to other heavy metal ions and few adsorbents are effective on Se(VI) adsorption.[24] The chemical reduction methods involve the use of ferrous hydroxide or zero-valence iron, which are expensive chemicals. With biological methods, bacteria help to reduce selenate and selenite into Se^0, however, a main challenge with this method is Se^0 will inhibit the

growth of bacteria.[25] Therefore, it is very necessary to find a cost-effective way for the removal of selenium. Photocatalysis turns out to be a promising way for the removal of selenium, especially selenate, as it reduces selenate directly to immobilized form of Se^0, which can be easily separated from the aqueous system.[26]

Semiconductors can function as photocatalysts under the irradiation of solar light energy that is more energetic than the bandgap energy of semiconductor.[27] Mechanism is shown in Fig. 3. Electron-hole pairs are formed in the conduction band and suitable redox potentials, which can be used for hydrogen evolution, oxygen reduction and reducing the hazardous contaminants for water treatment.[22, 28] Among all the semiconductors, TiO_2 is the most frequently used photocatalyst because of its favorable physical/chemical property, including high stability, nontoxicity and low cost.[29, 30]

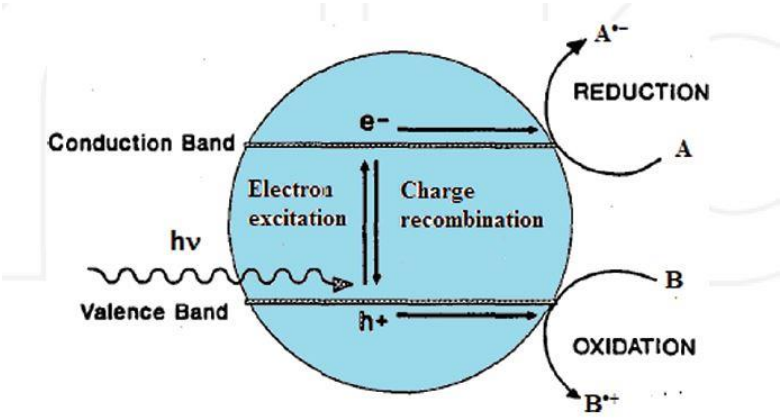

Fig. 3 Schematic illustration of the formation of photogenerated charge carriers (hole and electron) upon absorption of ultraviolet (UV) light[31]

Cr(VI) is present as dichromate at standard conditions(e.g., pH 0) and its reduction potential is E0 = 1.36 V vs. RHE. To be able to reduce Cr(VI), the semiconductors should have conduction band minima positive enough for the

photoreduction of Cr(VI) to occur. The valence band of the semiconductor should be more positive than the reduction potential for OH^-/O_2.[2]

The photocatalytic reduction of Cr(VI) happens on surface of the semiconductor between the redox couple of negatively charged $Cr_2O_7^{2-}$ or CrO_4^{2-} and positively charged $-OH_2^+$.[32] Electrons produced during the light irradiation will reduce Cr(VI) and the holes generated during the light irradiation will oxidize water or a sacrificial agent D^n. (Fig. 4) The chemical reaction under acidic condition(Eqs.1) and neutral condition(Eqs.2) are shown respectively as follows:[2]

$$2Cr_2O_7^{2-} + 16H^+ \rightarrow 4Cr^{3+} + 8H_2O + 3O_2 \quad (1)$$

$$4CrO_4^{2-} + 20H^+ \rightarrow 4Cr^{3+} + 10H_2O + 3O_2 \quad (2)$$

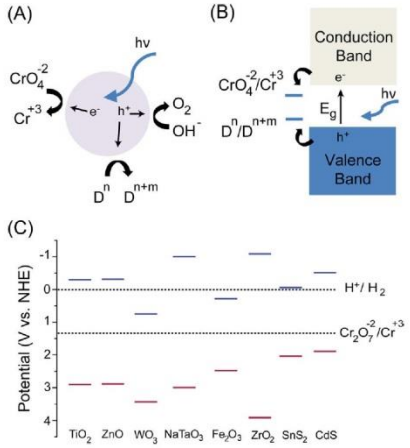

Fig. 4 (A) Schematic depicting photocatalytic reduction of hexavalent chromium

(B) Band diagram depiction of Cr(VI) photoreduction.

(C) Band edges for common semiconductor photocatalysts at standard conditions (pH 0) with respect to the redox potentials for H_2 generation and $Cr(VI)/Cr^{3+}$.[2]

In the context of photocatalytic reduction of selenate and selenite, electrons on conduction band of semiconductor will reduce selenate and selenite on surface of semiconductor to element Se, even H_2Se. Formic acid is usually used as hole scavenger.[20] What's more, the formic acid lowers the pH to acidic so the Se6 can bind on the TiO_2. It also can be oxidized by the photogenerated holes on TiO_2 rather than relying on water oxidation, which is kinetically slower. Dissolved oxygen in water solution will compete with selenium and be reduced to superoxideradicals, while water will be oxidized to highly oxidizing hydroxyl radicals.[26]

The mechanism for the photocatalytic reduction of Se is as follows:

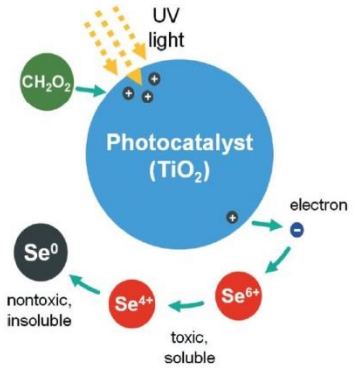

Fig.5 Schematic of Se^{6+} and Se^{4+} photoreduction by TiO_2 mechanism[20]

Methylene blue (MB), with its solution in blue color, is a kind of redox indicator in analytical chemistry. The photodegradation mechanism of MB accords to the dye degradation mechanism (Fig. 6). The first step is the photoexcitation of semiconductor. Take TiO_2 as example. TiO_2 is irradiated by photons with energy equal or greater than the band-gap energy of TiO_2. Then electron on valence band of semiconductor will migrate to conduction band and form a hole on valence band. The photogenerated hole will react with surface bonded water or OH^- to produce OH radicals, while the electrons on

conduction band will combine with the oxygen in water and form anionic superoxide radical(O^{2-}). Superoxide radical will first turn into hydroperoxyl radical (HO^{2-}) with the existence of proton and then turn into H_2O_2, which further dissociates into hydroxyl radicals (OH). The hydroxyl radicals will react with dye and finally produce CO_2 and H_2O.[33]

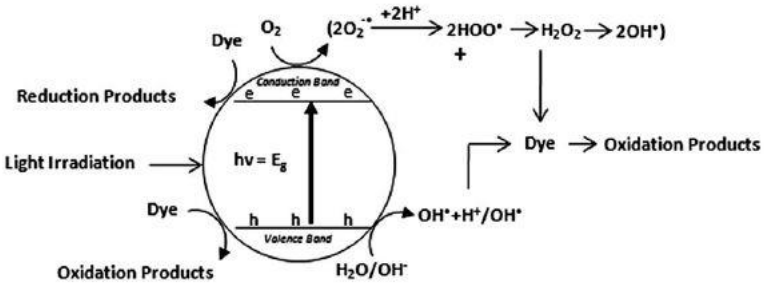

Fig. 6 Schematic of dye degradation by TiO_2 mechanism (under UV light)[33]

CHAPTER 2

LAYERED DOUBLE HYDROXIDE (LDH) NANOSHEETS WITH COMMERCIAL TIO_2 PARTICLE HYBRID MATERIALS

2.1 Overview of Layered double hydroxide based materials

Layered double hydroxides are a large family of two-dimensional anionic clay materials. It can be represented as $[M^{2+}_{1-x}N^{3+}_{x}(HO^{-})_2]^{x+}$ $[(X^{n-})_{x/n} \cdot yH_2O]^{x-}$, where M is a divalent metal, N is a trivalent metal, X is an exchangeable anion with a valence of n.[34] As shown in Fig. 7, metal anions exists in the layers, and a fraction of divalent metal anions are replaced by trivalent metal anions, which makes the layers positive charged.Water and exchangeable negative anions exist in the interlayers, compensating the positive charge in the layers. The interlayer bonding of LDH is relatively weak so it leads to other properties of LDH materials. For instance, the negative anions between layers are quite exchangeable with proper alternative anions.[35]

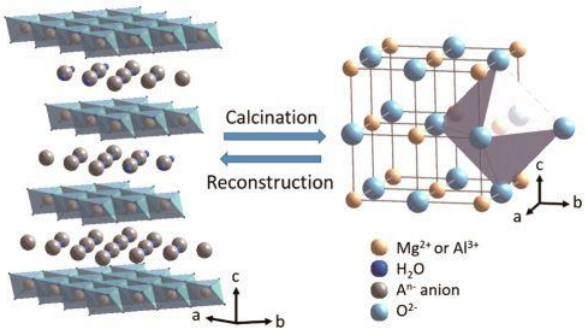

Fig.7 Crystal structure of layered double hydroxide and the pariclase structure formed after calcination. The layered structure is reconstructed upon exposure of the periclase structure to water.[36]

LDH is positively charged material so it can adsorb negatively charged chromate or selenium anions onto its surface or interlayers. MgAl-LDH has showed good adsorption towards selenium in our previous studies.[36] Besides, LDH has higher Point

Zero Charge (PZC) compared to TiO_2. TiO_2 is a semiconductor material which can act as photocatalyst, so the combination of LDH and TiO_2 will have more advantage than single LDH and single TiO_2. Better adsorption of LDH can benefit the photodegradation efficiency more than TiO_2. MgAl-LDH is tried first to form hybrid materials with TiO_2(P90), aiming at improving photodegradation efficiency by increasing the adsorption compared with only TiO_2(P90). To investigate the impact of morphology of LDH and the way of combination between LDH and TiO_2 on photoperformance of composites, three different type of LDH composites are synthesized.

2.2 LDH/TiO_2 hybrid materials

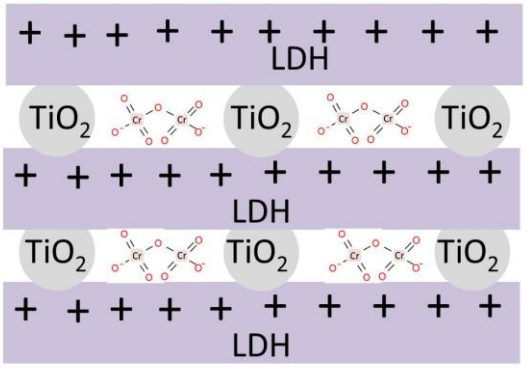

Scheme.1 Schematic of LDH nanosheets/TiO_2 hybrid materials for chromate removal

Scheme 1 is an idealized structure of how LDH and TiO_2 combined with each other. When UV light which has higher energy than bandgap of TiO_2 comes in, electrons on the valence band of TiO_2 will be excited to the conduction band of TiO_2, forming electron hole pairs on surface of TiO_2. Then chromate or selenate ions absorbed on surface of LDH will obtain free electrons on surface of TiO_2 and further get reduced.

2.2.1.1 Synthesis of commercial LDH and TiO_2 (P90) composites

100 mg of LDH (sasol) and 100mg of TiO_2 (P90) is dispersed in water separately. LDH is stirred for 5h and the sample not dispersed is sonicated for 15 min. TiO_2 (P90) is sonicated for a few seconds. Then TiO_2 dispersion is dropped into LDH dispersion and then stirred for 3h. The as-prepared composite is then filtered and dried in oven at 80 ℃.

2.2.1.2 Characterization of commercial LDH and TiO_2 (P90) composites

Previous studies in our group showed that after stirring or sonicating the Sasol LDH a homogenous suspension can be formed, shown in Fig. 8.[36] It indicates that after sonication Sasol LDH appears a nanosheet structure, with particle size around 200nm (from inset). From Fig.9, SEM image of TiO_2 (P90), we can see that P90 is in small and uniform particle size. After combination the hybrid material looks like bulk morphology, as shown in Fig.10. EDS mapping (Fig.11) is performed and from the images we could conclude that LDH and TiO_2 mixed with each other uniformly. The intimate contact between LDH and TiO_2 will benefit the photodegradation efficiency of hybrid materials towards selenium and chromium.

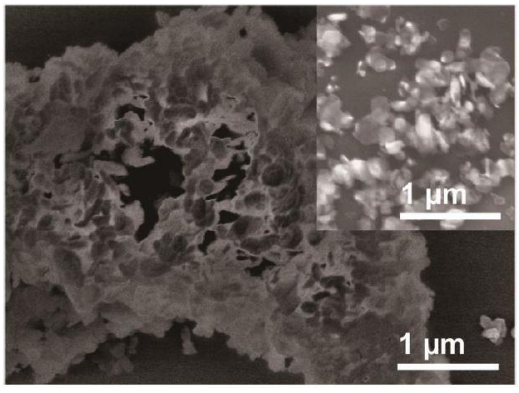

Fig.8 SEM image of granular LDH; particles obtained after sonication shown in inset

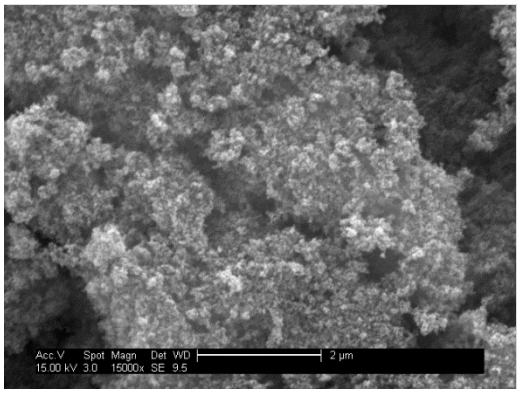

Fig.9 SEM image of TiO_2 (P90)

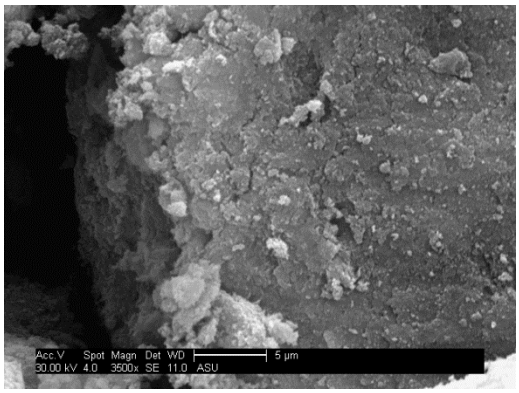

Fig.10 SEM image of commercial LDH (sasol)/TiO_2 (P90) composites

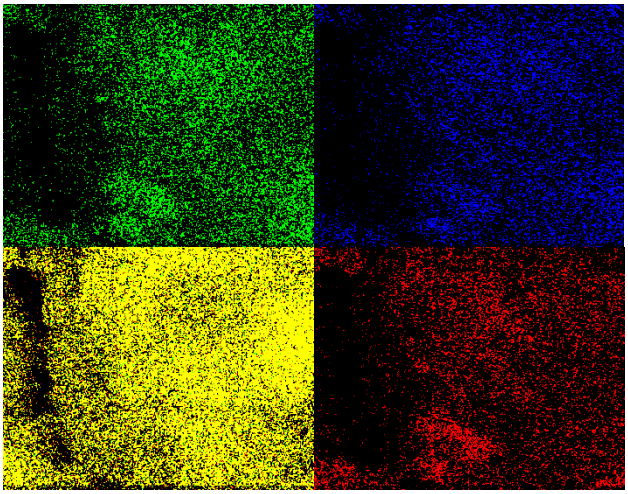

Fig.11 EDS mapping of commercial LDH (sasol)/TiO_2 (P90) composites (Mg in green, Al in blue, Ti in yellow and O in red)

2.2.1.3 Photoreduction and dark adsorption results of selenium with commercial LDH (Sasol)/TiO_2 composite

1 g/L of Se(VI) solution is prepared by dissolving Na_2SeO_4(Sigma-Aldrich) into DI water as stock solution. 150 mg of composite is put into 150 ml of 1ppm Se(VI) solution respectively for the photoreaction and dark adsorption. Samples at time 0 min are taken before the composites are put into the Se (VI) solution. Samples at time 30s are taken after LDH/TiO_2 composites are put inside the water and stirred for 30s. The rest samples are taken every 15 min within 2 hours. Since dissolved oxygen might compete with Se(VI) for the electrons on the conduction band, and forms superoxide radical anions.[25] Nitrogen is purged into the Se (VI) solution for 1 h to evacuate oxygen from the system before composites are put inside the solution. And also, nitrogen is purged during the whole photoreaction and dark adsorption. The reactions are performed inside the Quartz tube within the UV reactor (Rayonet RRP-200 photochemical reactor, light source of 1.65 x 10^{16} photons/sec/cm^3 at λ = 350 nm). The concentration of selenium is analyzed with inductively coupled plasma mass spectrometry (ICP-MS, iCap Q quadrupole, Thermo Co., USA) at ASU.

Dark adsorption of LDH and TiO_2 (P90), dark adsorption and photoreduction of TiO_2(P90), and also dark adsorption and photoreduction of selenate with the commercial LDH/TiO_2 composites (weight ratio 1:1) are shown in Fig.12a, Fig. 12b, and Fig. 12c respectively. Fig. 12a shows that both LDH and TiO_2 (P90) alone performs great adsorption to selenate. Almost all selenate could be removed from the beginning. Fig. 12b shows the photoreduction performance of TiO_2 (P90) is affected by Ar flow. Since the hybrid material also has adsorption ability, for comparison, control test of dark

adsorption under the same condition was performed. The results indicate that there is no obvious difference between the dark adsorption and photoreduction performance. We expect that when UV light exists, Selenate could be removed faster than under the condition of control test. Further experiments need to focus more on the mechanism of selenate photodegradation.

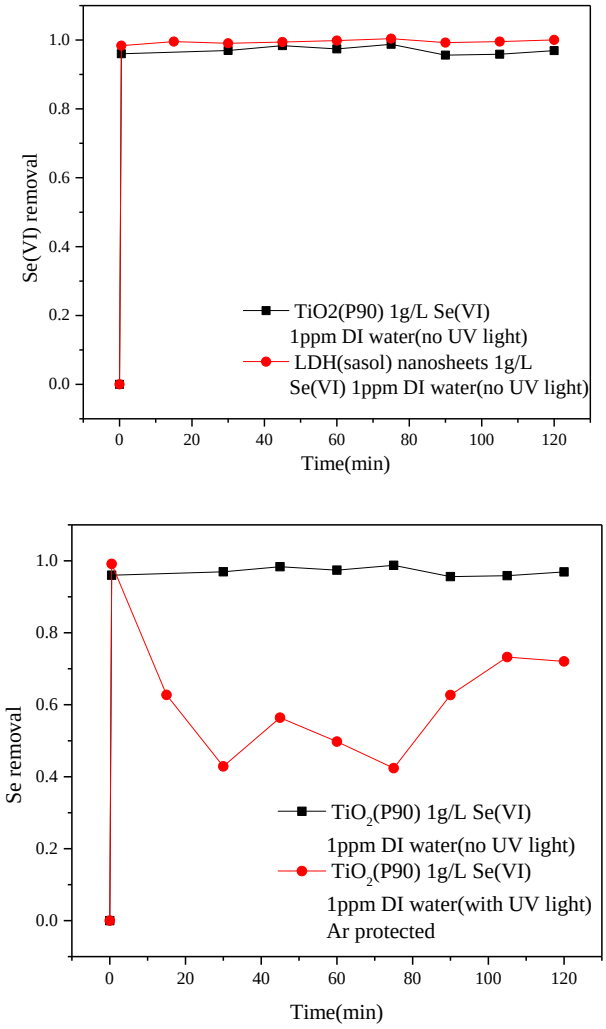

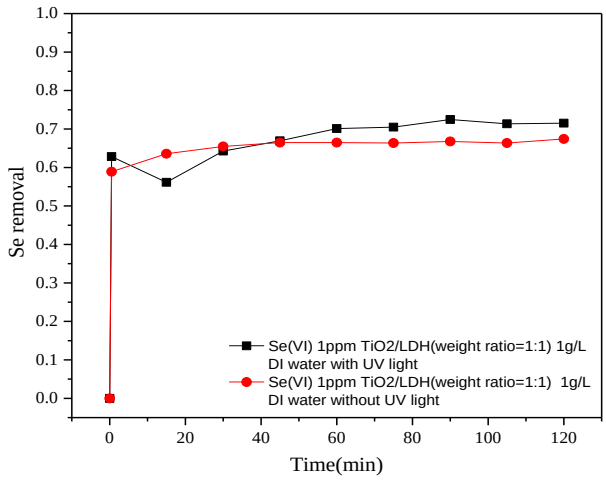

Fig. 12a Dark adsorption curve of commercial LDH (sasol) and TiO_2 (P90) towards selenate; b Photoreduction and dark adsorption curve of TiO_2 (P90) composites towards selenate; c Photoreduction and dark adsorption curve of commercial LDH (sasol)/TiO_2 (P90) composites towards selenate

2.2.2 Homemade LDH nanosheets/TiO_2 composites

Since the morphology of commercial Sasol LDH is different with the morphology of homemade LDH, in order to compare the influence of morphology of LDH on the impact of photoperformance, we further tried to synthesize LDH nanosheets in the lab instead of using commercial LDH to understand more about the impact of LDH on photodegradation of environmental pollutants. We tested the photodegradation ability of homemade LDH nanosheets with TiO_2 (P90) hybrid materials towards chromate.

2.2.2.1 Synthesis of homemade LDH and TiO_2 (P90) composites

Synthesis of homemade LDH

Based on the method reported by Xu et al, $Mg_2Al(OH)_6Cl\ xH_2O$ was prepared.10 mL of mixed salt solution containing $MgCl_2$ (3.0 mmol) and $AlCl_3$ (1.0 mmol) was added within 5 s into a 40 mL NaOH solution (0.15 M) under vigorous stirring, followed by 10-

30 min stirring with the reactor isolated from air. Pure LDH slurry was obtained via centrifuge separation and washing, and then manually dispersed in 40 mL of deionized water and hydrothermally treated in an autoclave at 100 ℃ for 16 h, resulting in a stable homogeneous suspension.[37]

Synthesis of homemade LDH/TiO_2 composites

Firstly, pH of DI water is adjusted to 10 with NaOH. TiO_2 (P90) is suspended into water and sonicated for half an hour to form a 2.33 g/L TiO_2 collidal solution. Then TiO_2 collidal solution is dropped into LDH suspension slowly under the protection of N_2. The final LDH amount in LDH/TiO_2 product is 12% and 50% respectively.

2.2.2.2 Characterization of homemade LDH nanosheets/TiO_2 composites

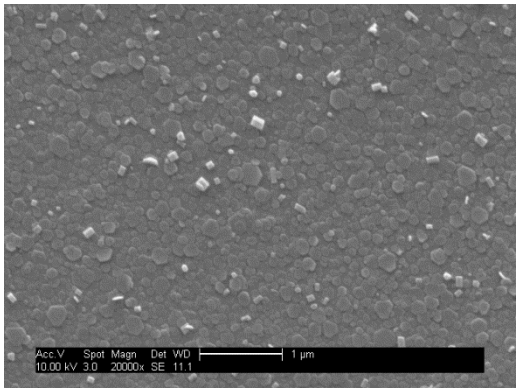

Fig.13 SEM image of homemade LDH nanosheets

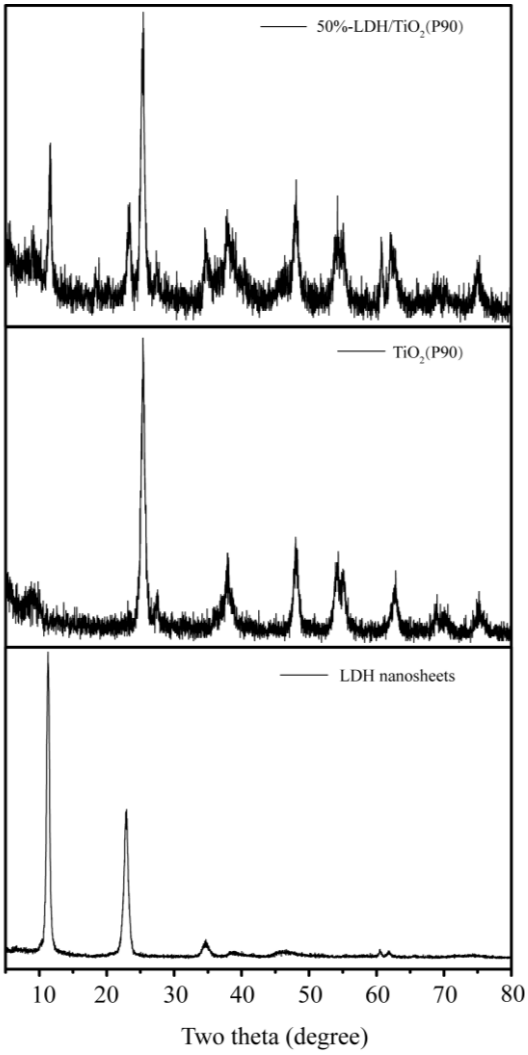

Fig.14 XRD pattern of homemade LDH nanosheets, TiO_2 (P90) and 50%-LDH/TiO_2 (P90) composites

Homemade LDH suspension is dipped onto silicon substrate and dried under room temperature for SEM characterization. From SEM image of homemade LDH (Fig. 13), it is observed that homemade LDH is uniformly distributed on surface of silicon substrate with particle size ranged from around 50 nm to 300 nm. XRD pattern of LDH nanosheets is consistent with the reference.[37] XRD pattern of 50%-LDH/TiO_2 (P90) (Fig.

14) shows the characteristic peaks of both TiO_2 (P90) and LDH nanosheets, indicating that TiO_2 (P90) and LDH is combined with each other successfully.

2.2.2.3 Photoreduction results of chromate(Cr(VI)) with LDH/TiO_2 composites

The Cr(VI) reduction with TiO_2 nanosheets is performed under UV light. Initial Cr(VI) solutions were prepared by dissolving $K_2Cr_2O_7$ in ultrapure DI water (18.3 MΩ-cm) at a concentration of 10 ppm. Then 1 g/L photocatalyst is dispersed into the Cr(VI) solution. The photocatalytic experiment is performed after dark adsorption for 30 min in a long quartz tube inside the Rayonet RRP-200 photochemical reactor (Southern New England Ultraviolet Company) with light source of 1.65 x 10^{16} photons/sec/cm^3 at λ = 350 nm. Samples are taken every 15 min within 2 h. The concentration of Cr(VI) solution was determined with TNT 854 reagent kit from Hach by measuring the maximum light absorbance (at 543 nm) with a UV–vis spectrophotometer (Ocean-opticsDH-2000-BAL). The mechanism for the Cr(VI) test method is as follows: Cr(VI) reacts with 1,5-diphenylcarbazide and forms 1,5-diphenylcarbazone. The amount of red color formed with hexavalent chromium is directly proportional to the amount of chromium in the sample. (https://www.hach.com/chromium-tntplus-vial-test-0-03-1-00-mg-l-cr/product-parameter-reagent?id=7640179469&callback=qs)

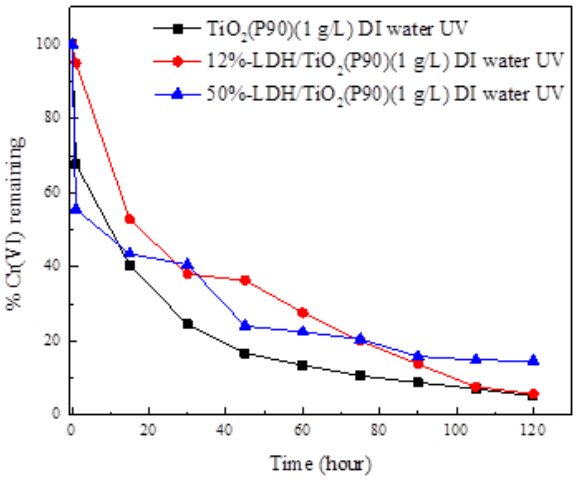

Fig.15 Photoreduction curves of homemade LDH /TiO_2 (P90) composites towards chromate

The photoreduction performance of TiO_2 (P90), 12%-LDH/TiO_2 (P90) composite and 50%-LDH/TiO_2 (P90) composite are as in Fig. 15. TiO_2 (P90) can remove about 85% of chromate in the solution after 1 h and almost all the chromate after 2 h. 12%-LDH/TiO_2 (P90) composite can remove about 70% of the chromate after 1 h and 50%-LDH/TiO_2 (P90) composite can remove about 75% of the chromate after 1 h. Both hybrid materials give a worse performance than TiO_2 (P90). When part of the TiO2(P90) is replaced by LDH, the LDH are expected to absorb Cr(VI) more effectively and the intimate contact between TiO_2(P90) and LDH will make TiO_2(P90) reduce the absorbed Cr(VI) more quickly. But the weight ratio of TiO_2(P90) in the photocatalysts decreased so that the photoreduction effeciency also decreased.

2.2.3 In-situ LDH/TiO_2 composites

Both commercial LDH and homemade LDH with TiO_2 (P90) hybrid materials don't reach our expectation of improving the photodegradation efficiency of environmental pollutants (selenium, chromium). We further tried to use in-situ growth of

LDH onto TiO_2 (P25). The sample is from our project collaborator, Minjeong Suh and Jaehong Kim at Yale University. We acknowledge Minjeong and Jaehong for providing the samples. The in-situ synthesis method will create a much more intimate contact between TiO_2 and LDH materials. There are hydrogen bondings between LDH and TiO_2 instead of just simple mixture. In their studies they found better improvement for dye degradation in the composite, so we expect the material will also show a better performance on the photodegradation of selenate. So we tested its photodegradation ability on selenate.

2.2.3.1 Preparation of in situ LDH/TiO_2 composites:

The synthesis of in situ LDH/TiO_2 composites was prepared by collaborators at Yale by taking $Mg(NO_3)_2.6H_2O$ (1.71 g), $Al(NO_3)_3.9H_2O$ (1.25 g) and urea (5.20 g) were dissolved in deionized water to form a clear solution with a total volume of 100 mL.[38] Add (varying amounts of) P25 to the stock solution in a Teflon-lined stainless steel autoclave, and stir and sonicate the resulting mixture to ensure that the P25 is uniformly dispersed. Place the autoclave in an oven at 90 ^oC for 9h (ramp rate of 5 ^oC/min used). Wash the composite material with deionized water a number of times to remove the residual urea on the material surface.

2.2.3.2 Photoreduction of selenium with LDH/TiO_2 composites

30% TiO_2/LDH composite is tested. 150 mg of composite is put into 150 ml Se(VI) solution respectively for the photoreaction and dark adsorption. Samples at time 0 min are taken before the composites are put into the Se(VI) solution. Samples at time 30s are taken after LDH/TiO_2 composites are put inside the water and stirred for 30s. The rest samples are taken every 15 min within 2 hours. Nitrogen is purged into the Se(VI)

solution for 1 h before composites are put inside the solution and also purged during the whole photoreaction and dark adsorption. The reactions are performed in the beaker with the UV lamp (UVP, 8 Watt, 0.16 Amps, 115V, 60 HZ, wavelength 254 nm) above the solution. The concentration of selenium is analyzed with inductively coupled plasma mass spectrometry (ICP-MS, iCap Q quadrupole, Thermo Co., USA) at ASU. Photoreduction performance of selenate with the in situ LDH/TiO_2 hybrid material is in Fig. 16. Since the hybrid material also has adsorption ability, for comparison, control test of dark adsorption under the same condition was performed. The results indicate that there is no obvious difference between the dark adsorption and photoreduction performance. When there is UV light existing, the speed of Se(VI) removal is not faster than under the dark condition. It means that the existence of UV light didn't result in any photoreaction. Further experiments need to focus more on the mechanism of selenate photodegradation.

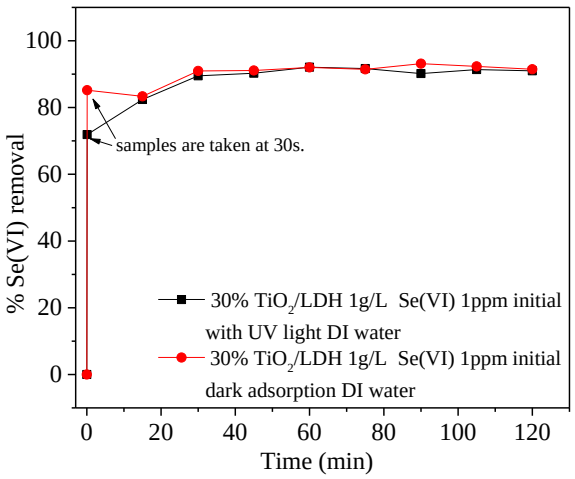

Fig.16 Photoreduction and dark adsorption curve of in-situ LDH/TiO_2 (P90) composites towards selenate

CHAPTER 3

TIO_2 NANOSHEETS

3.1 Overview of TiO_2 nanosheets

We synthesized LDH/TiO_2 composites using commercial TiO_2 and then tried to combine with LDH. We tried homemade and commercial LDH and also in situ synthesis method. However, none of those methods is promising as photocatalysts to remove Se(VI) or Cr(VI). The problems are that the TiO_2 are agglomerated with LDH and one possible way to solve this problem is to use sheet structure.

Materials with layered (or lamellar) structures can be more easily prepared with platelet or sheet-like morphologies due to the natural bonding anisotropy in the intra- and interlayer directions, but anatase does not exhibit such a layered structure. Platelet-type nanocrystals of anatase have been successfully prepared using hydrothermal methods, but fluoride anions, typically from toxic reagents such as hydrofluoric acid, must be used as a structure-directing agent.[39, 40] For instance, Yang et al[41] used titanium tetrafluoride(TiF_4) as precursor and synthesized TiO_2 nanosheets with dominant facets using a hydrothermal method. Han et al[40] reported titania nanosheets with a high percentage of exposed (001) facets with tetrabutyl titanate as precursor and hydrothermal method. Hydrofluoric acid is utilized in both of their synthesis procedures. Nanosheet-type structures with larger lateral dimensions have also been demonstrated by converting nanosheets of layered, lepidocrocite-type titanate compounds to anatase using hydrothermal or calcination treatments.[42-45] While the conversion of these titanates to the anatase structure has been found to be topochemical in nature, the layered titanate nanosheets must be obtained by exfoliation using osmotic swelling, which is a multi-step process involving ion-exchange

and intercalation of bulky ammonium cations.[46] For example, Gunjakar et al[47] reported using the layered cesium titanate as precursor and tetrabutylammoniu for exfoliation and obtained exfoliated titanate nanosheets. Previous work exploring exfoliation-based methods for obtaining energy storage materials in 2D morphologies have shown that these large organic cations are strongly adsorbed on the nanosheet surfaces and can interfere with their interfacial properties unless they are removed using electrophoresis.[48, 49]

To our knowledge, the preparation of TiO_2 nanosheets from the conversion of TiS_2 nanosheets has not been explored. This approach is attractive, as the preparation of 2D nanosheets using chemical and electrochemical reduction methods has been demonstrated for a large number of layered, transition metal dichalcogenide materials[50, 51] and hence has the opportunity to lead to a large number of layered metal oxides. Additionally, using TiS_2 as the starting material can enable sulfur-doped TiO_2, which has a smaller bandgap than pure anatase and enhanced photocatalytic properties.[52-56]

3.2 Synthesis of TiO_2 nanosheets

The TiS_2 nanosheets were synthesized first via the electrochemical exfoliation of bulk TiS_2 similar to the method described elsewhere.[57] The lithium intercalation of TiS_2 was performed in pouch cells with lithium foil as the counter anode. The working electrode was prepared by mixing TiS_2, carbon black, and PVDF binder in a weight ratio of 8:1:1 under vigorous stirring for 12 h with N-methylpyrrolidone (NMP) as dispersant. The slurry was cast onto copper foil and dried at 120 ℃ for 12 h. Pouch cells were assembled in an argon-filled glovebox. The assembled cells were discharged galvanostatically using a 0.05 C rate (assuming a theoretical lithiation capacity of 239

mAh/g) to 0.9 V vs. Li/Li^+ using a BioLogic VMP3 potentiostat. Then the electrode was held at 0.9 V for 2 h, followed by a 1.5 h rest at open circuit. If the voltage was higher than 1V, the electrode was charged galvanostatically again using a 0.05 C rate until the potential reached 0.9 V vs. Li/Li^+, then another 2 h was held at 0.9 V. The step was repeated until the open circuit voltage was less than 1V. The lithiated TiS_2 cathode was dispersed in ice water and sonicated for 1 h (with the ice water used to mitigate heating from the sonication and avoid agglomeration of the nanosheets). Afterwards, the resulting suspension was centrifuged at 3000 rpm for 20 min to separate the TiS_2 nanosheets (dispersed in water solution) and unreacted materials (agglomerated on the bottom).

To prepare TiO_2 nanosheets, O_2 from a gas cylinder was purged into the as-prepared TiS_2 solution for 30 min to 1 hour to ensure sufficient dissolved O_2 for the reaction with TiS_2. The O_2 purged dispersion was then put into 40 mL autoclave vessels (Parr) with each vessel containing a maximum of 30 mL of solution. The pre-treated TiS_2 nanosheet dispersion was hydrothermally reacted at 180 ℃ for 14 h to obtain the TiO_2 nanosheets.

The crystal structure of the TiO_2 nanosheets was determined using X-ray diffraction (XRD) under monochromatic Cu Kα radiation (λ=1.5405 Å) (Panalytical X′pert Pro). The size and morphology of the materials were observed using scanning electron microscopy (SEM) using a FEI XL 30 field emission SEM, transmission electron microscopy (TEM) using a Philips CM200 microscope, and atomic force microscopy (AFM) using a Bruker Multimode scanning probe microscope. X-ray photoelectron spectroscopy (XPS) was performed on a VG ESCALAB 220i-XL with Al Kα anode (1486.6 eV) operated at 63 W and 15 kV. The X-ray takeoff angle was 45^o and

the data were acquired from the region within ~500 μm of the outer surface of the sample. Charge compensation was used because TiO_2 is a wide bandgap semiconductor. A pass energy of 20 eV was used for high-resolution spectra. The spectra were calibrated to the C 1s hydrocarbon peak at 284.7 eV. Peak fitting was performed using CasaXPS processing software. Raman spectroscopy was performed in air at room temperature using a WITec alpha 300R confocal Raman microscope system, using a 100X objective lens and 532 nm excitation laser.

3.3 Schematic of TiO_2 nanosheets

In the current work, the synthesis of TiO_2 nanosheets was established with a three-step process (Fig.17). The first step involves the reduction of bulk TiS_2 material through electrochemical lithiation to form Li_xTiS_2, using procedures similar to those used when utilizing TiS_2 as a positive electrode in a Li battery.[58] An example voltage profile for the lithiation of the TiS_2 electrode is shown in Fig.18. The lithiation weakens the van der Waals interaction between the TiS_2 interlayers and enables exfoliation via ultrasonication. The exfoliated TiS_2 nanosheets are uniformly dispersed in water (Fig. 19). Then, the as-obtained TiS_2 nanosheet dispersion is oxidized using a hydrothermal treatment to obtain TiO_2 nanosheets. Previous studies TEM studies showed that the oxidation product of TiS_2 after immersion in de-ionized water solutions was amorphous,[59] so the hydrothermal treatment is implemented here to improve the crystallinity of the formed TiO_2.

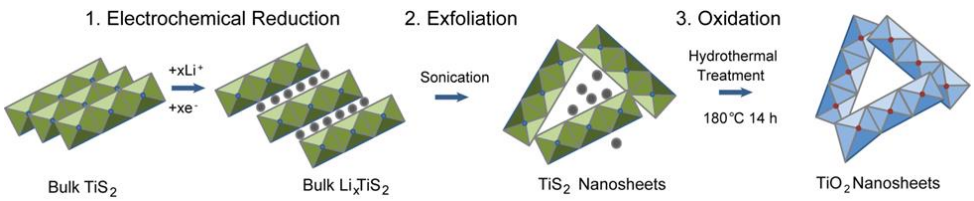

Fig.17 Synthetic procedure for the preparation of TiO_2 nanosheets

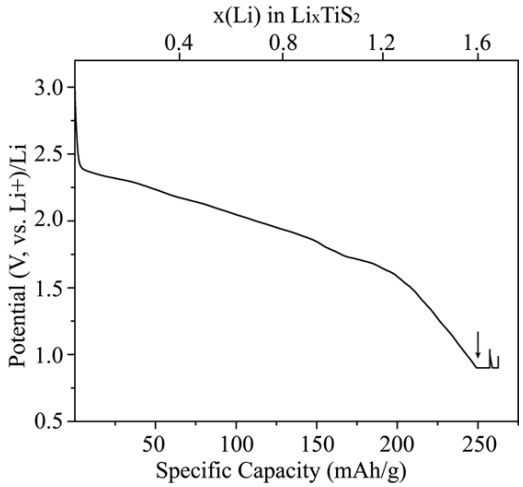

Fig.18 Lithiation voltage profile of bulk TiS_2. The electrode was charged galvanostatically using a 0.05 C rate until the potential reached 0.9 V vs. Li/Li^+, as indicated by the arrow. Then the electrode was held at 0.9 V for 2 h, followed by a 1.5 h rest at open circuit. If the voltage was higher than 1 V vs. Li/Li^+ after this relaxation period, the electrode was charged galvanostatically again using a 0.05 C rate until the potential reached 0.9 V vs. Li/Li^+, followed by another 2 h potentiostatic hold at 0.9 V. These steps were repeated until the open circuit voltage was less than 1 V vs. Li/Li^+.

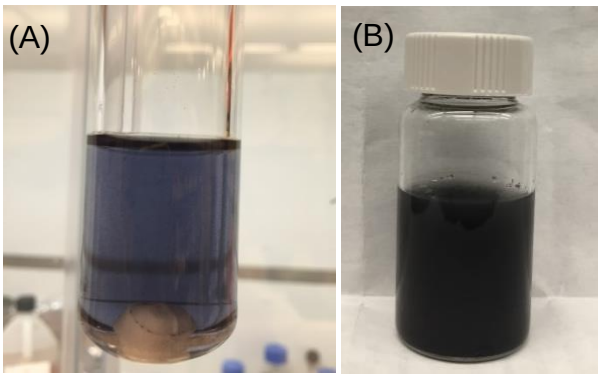

Fig. 19 Photographs of (A) dispersed Li_xTiS_2 nanosheets obtained after electrochemical lithiation of bulk TiS_2, and (B) TiO_2 nanosheets obtained after hydrothermal treatment.

3.4 Characterization of TiO_2

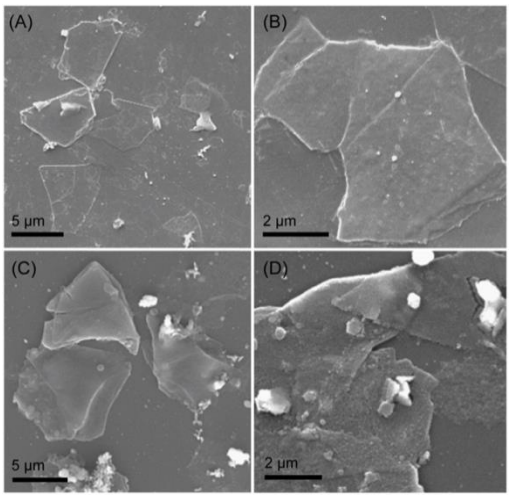

Fig.20 SEM images of (a, b) exfoliated TiS_2 nanosheets, (c, d) prepared TiO_2 nanosheets.

The scanning electron microscopy (SEM) images of the exfoliated TiS_2 nanosheets and prepared TiO_2 are shown in illustrated in Fig. 20. The lateral size of the TiS_2 nanosheets varied from 2 to 10 μm (Fig. 20a-b). From Figure 20c-d, it can be seen that the TiO_2 nanosheets obtained after hydrothermal treatment could maintain the sheet-like morphology of the TiS_2 starting materials. However, in addition to the nanosheets materials, some agglomerated particles and residues were observed on the substrate. Raman spectroscopy and high magnification optical microscopy was used to characterize the samples (Fig. 21). The Raman spectrum taken from the nanosheet region displayed a peak at about ~150 cm^{-1}, which matches the E_g mode of anatase.[60] The intensity of this peak was still present, but much weaker when obtaining a spectrum from the residue on the background, which suggests that the residue consists of some anatase but probably mostly carbonaceous material such as the carbon black and PVDF binder from the TiS_2 electrode.

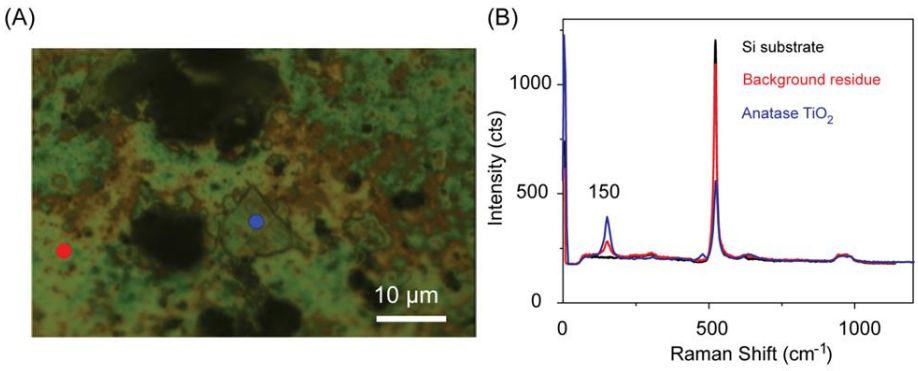

Fig. 21 Raman spectroscopy analysis of prepared TiO_2 nanosheets. (A) Optical microscopy image with blue spot localized on a TiO_2 nanosheet and red spot on carbon residue on the background. (B) Corresponding Raman spectrum from the red and blue spots in (A). The peak at 150 cm^{-1} is from the E_g mode of anatase while the large peak at 520 cm^{-1} is from the crystalline Si substrate.

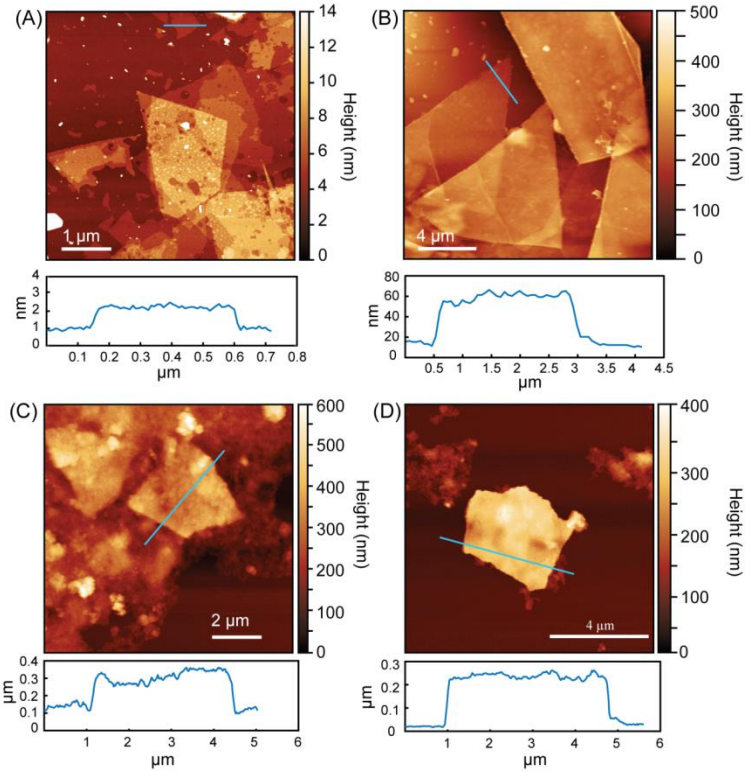

Fig.22 AFM images of of (a, b) exfoliated TiS_2 nanosheets, (c, d) prepared TiO_2 nanosheets.

The thickness of TiS_2 and TiO_2 nanosheets were measured using atomic force microscopy (AFM). The AFM images show that the thickness of the exfoliated TiS_2

nanosheets ranged from around 1 nm to 40 nm (Figure 22a-b). According to previous work, single-layer TiS_2 nanosheets should have a thickness of 0.9 – 1.2 nm,[57] which indicates that the TiS_2 samples were a mixture of single and multi-layered nanosheets. This is likely due to the wide distribution of particle sizes in the starting TiS_2 materials (Fig. 23), with the smaller particles sizes leading to more complete exfoliation. It was also observed that the lateral size of the TiS_2 nanosheets varied from very small pieces to around 10 μm, which is in accordance with the SEM images (Fig. 20a-b). The AFM images of the as-prepared TiO_2 nanosheets was determined to be around 200 nm to 240 nm (Fig. 22c-d). The increase in thickness compared to the TiS_2 nanosheets could be caused by agglomeration or restacking of the sheets during the hydrothermal treatment.

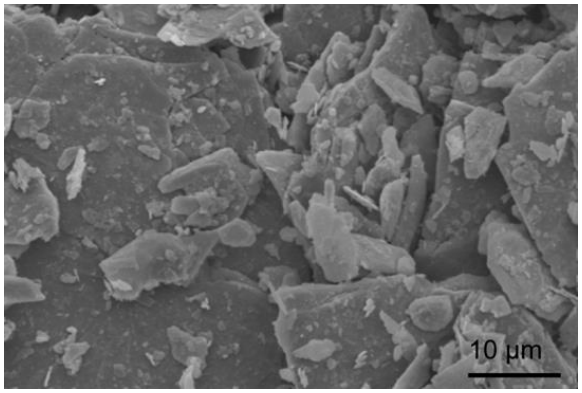

Fig.23 SEM images of as-received, bulk TiS_2.

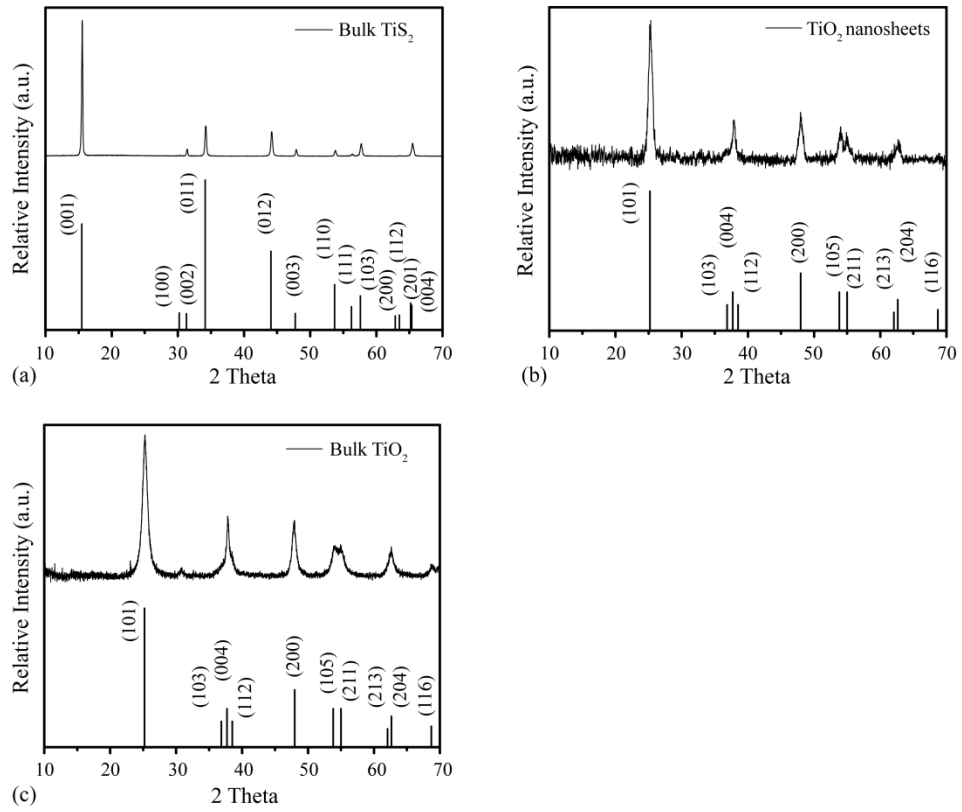

Fig. 24 XRD pattern of (a) as-received, bulk TiS2, (b) as-prepared TiO_2 nanosheets obtained after hydrothermal treatment of TiS2 nanosheets, and (c) as-prepared bulk TiO_2 obtained after hydrothermal treatment of bulk TiS2. The reference patterns for TiS2 and TiO_2 were obtained from JCPDS No.15-0853 and JCPDS No. 21-1272, respectively.

To better understand the structure of the TiO_2 nanosheets, X-ray diffraction (XRD) and high resolution transmission electron microscopy (TEM) were performed. The XRD pattern (Fig. 24a) of the bulk TiS_2 starting material matched that expected for the hexagonal structure of TiS_2 with close agreement with the reference pattern for anatase (Fig. 24b), suggesting no preferential crystalline orientation. No additional diffraction peaks were observed, indicating that the transformation of the TiS_2 nanosheets to TiO_2 did not result in other crystalline phases. Performing the same hydrothermal treatment on bulk TiS_2 particles (without exfoliation into nanosheets) also resulted in formation of bulk anatase TiO_2 as verified by XRD (Fig. 24c), confirming the oxidation through this process.

The TEM results showed that the TiO_2 nanosheets were polycrystalline, which is consistent with the XRD pattern. From the TEM image in Fig. 25a, the sheet-like morphology of the TiO_2 is easily identified, but it is composed of many small crystallites. The high resolution TEM image in (Fig. 25b) shows the polycrystalline nature of the TiO_2 nanosheets. The lattice spacing of 0.35 nm was measured, which is close to the *d*-spacing for the (101) atomic planes of anatase TiO_2. These results show that while the morphology of the initial TiS_2 nanosheets was maintained during the hydrothermal treatment, the formed anatase was polycrystalline due to the differences in bonding arrangements between the TiS_2 and anatase crystal structures. TiS_2 is comprised of Ti-S octahedra arranged in "slabs" with sulfur atoms separated with van der Waals bonding, which results in layers of Ti atoms sandwiched between two sulfur layers.[61] On the other hand, anatase is comprised of edge sharing, distorted Ti-O octahedral[62] and lacks a similar van der Waals gap that enables both the facile Li insertion and exfoliation in TiS_2. Hence, the structural rearrangement during the oxidation process results in the formation of polycrystalline materials, but interestingly still enables the nanosheet morphology to be maintained.

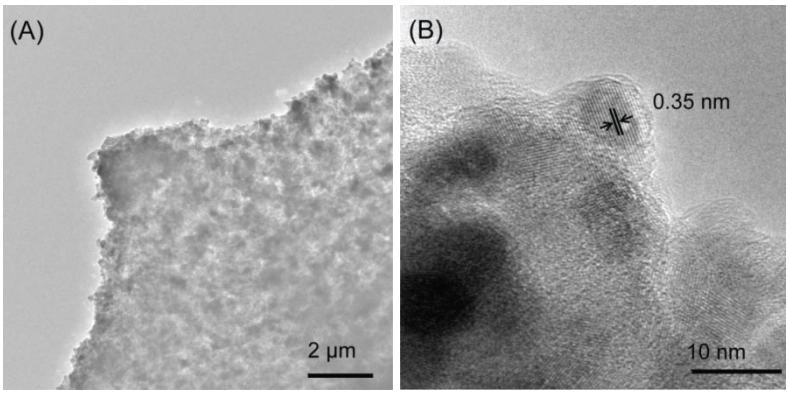

Fig. 25 (A) TEM and (B) high resolution TEM images of TiO_2 nanosheets.

X-ray photoelectron spectroscopy (XPS) was used to characterize the chemical states in the TiO_2 nanosheets. Fig. 27 shows the Ti 2*p*, O 1*s* and S 2*p* XPS spectra obtained from the surface of the TiO_2 nanosheets. These peaks are found at lower binding energies 456.4 and 462.4 eV in TiS_2[63] and can be well distinguished from the Ti-O peaks in samples comprised of partially oxidized TiS_2.[64, 65]

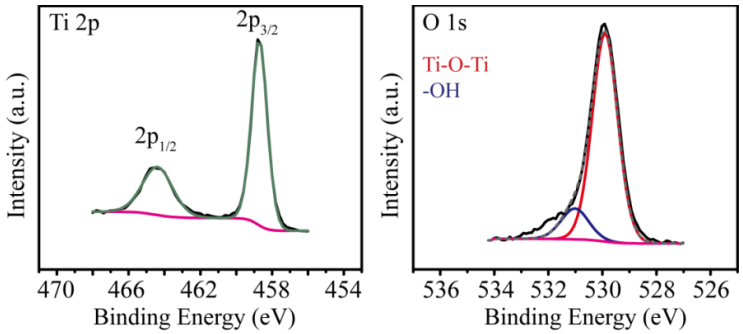

Fig. 26 XPS peaks of P25 (align to C1s 284.7 eV)

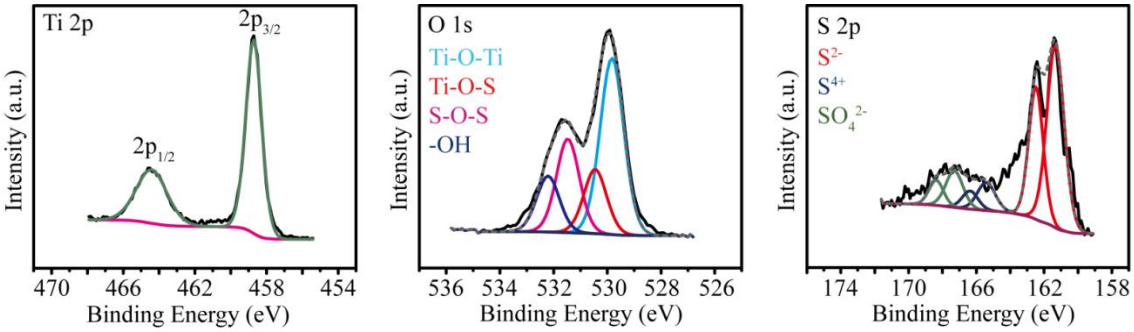

Fig. 27 XPS peaks of TiO_2 nanosheets (align to P25 O1s 529.89 eV)

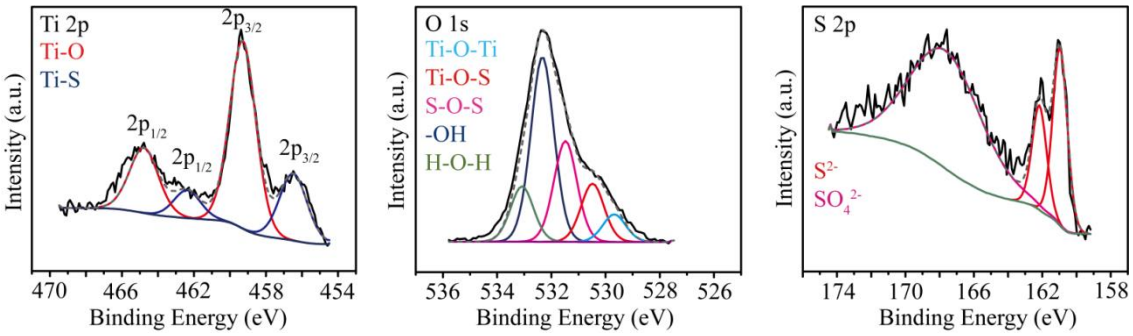

Fig. 28 XPS peaks of TiS_2 nanosheets (align to C1s 284.7 eV)

Since we do not observe the separation of the peaks in our results, this indicates that the TiS_2 was successfully converted to TiO_2. The O 1s XPS spectrum showed two peaks, with the peak at 530.9 eV attributed to the Ti-O bond in the TiO_2, and the peak at higher binding energy (532.5 eV) attributed to the surface hydroxide. The presence of S 2p XPS signal indicated that there was still some sulfur remaining after the hydrothermal treatment. The S 2p peaks for S^{2-} are found at 161.97 and 160.85 eV in TiS_2.[63] Hence, this implies that some Ti-S bonds are still present in the TiO_2 nanosheet samples. The broad peak at 168.38 eV is associated with S^{4+} that there is still some S remaining after hydrothermal treatment. The absence of a peak at 169 eV, which is associated with S^{6+},[53] indicates that Ti^{4+} is not substituted with S^{6+}.

3.5 Photodegradation of MB (methylene blue) with TiO_2 nanosheets

3.5.1 Photodegradation procedure of MB (methylene blue) with TiO_2 nanosheets

The photocatalytic activity of as-prepared TiO_2 nanosheets was evaluated by photodegradation of MB (methylene blue) in aqueous solution under UV irradiation. UV spectrophotometer (UVP, 8 Watt, 0.16 Amps, 115V, 60 HZ) at its characteristic wavelength 254 nm was used as light source to determine the degradation. All the photocatalytic reactions were performed in 50 mL glass beaker under magnetic stirring with UV light illuminated above the surface of aqueous solution. The UV light source was turned on 2 h ahead of the photoreaction. 0.2 g/L as initial concentration of photocatalysts was added into 30 mL solution containing 5 ppm MB. Dark adsorption was carried out for 10 h before photo reaction to reach adsorption-desorption equilibrium between the photocatalysts and MB. About 2 mL of suspension were taken at certain time

intervals during the photoreaction and centrifuged to remove the photocatalysts to obtain clear MB solution. The concentration of MB in the collected samples was determined by UV-vis spectroscopy through measuring absorbance at a wavelength of 664 nm. Each photoreaction with the same kind of photocatalyst was repeated 2 times to determine the reproducibility of the results.

To evaluate the effect of carbon black and PVDF inside the TiO_2 nanosheets materials on photodegradation of MB, P25, carbon black in a weight ratio of 9:1 (P25+carbon black)and also P25, carbon black and PVDF in a weight ratio of 9:1 (P25+ carbon black+ PVDF) were mixed and hydrothermal treated at 180 C for 14 h.

3.5.2 Photodegradation results of MB (methylene blue) with TiO_2 nanosheets

The effect of TiO_2 nanosheets on the photodegradation of MB was shown in Fig. 29. Photodegradation of MB by P25, P25 + carbon black (PC), and P25 + cabon black + PVDF (PCP) were also evaluated at same conditions for comparison. The results indicate that P25 shows a faster degradation towards MB than TiO_2 nanosheets. The P25 can remove almost all the MB inside the solution within 22 min, but with the TiO_2 nanosheets MB still remains 12.77% after 20 min of irradiation. However, the degradation speed of both PC and PCP are slower than TiO_2 nanosheets. From this result we can deduce that carbon black and also PVDF inside the TiO_2 nanosheets material have a negative impact on the photodegradation of MB. The first reason might be the carbon black and PVDF are both hydrophobic so that they inhibit the intimate contact of photocatalyst with water, which further inhibit the contact of photocatalyst and MB inside the water. The second reason might be the existence of carbon black and PVDF cause the agglomeration of the materials, which also reduces the active surface area of photocatalysts for photoreaction.

We can further infer that if carbon black and PVDF can be successfully removed from the TiO_2 nanosheets material, the TiO_2 nanosheets is a very promising photocatalytic material on the photodegradation of MB. Fig. 30 shows the kinetics of disappearance of MB for all the photocatalysts. The first order equation: Ln(Cinitial/C) = kt was used to fit the data in Fig. 29. It is obvious that fitted degradation curves for all the photocatalysts follows the first order model, which is similar with other studies. The rate constants are 0.185 min^{-1} for P25, 0.1026 min^{-1} for TiO_2 nanosheets, 0.0707 min^{-1} for PC and 0.0705 min^{-1} for PCP respectively (Table 1).

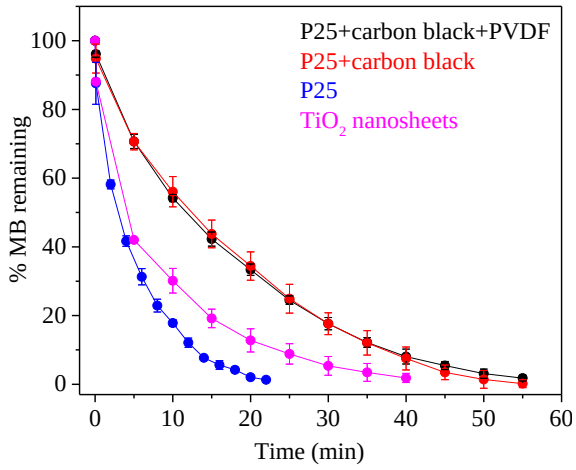

Fig. 29 Degradation curves of MB by photocatalysts (P25, TiO_2 nanosheets, PC and PCP) under UV irradiation

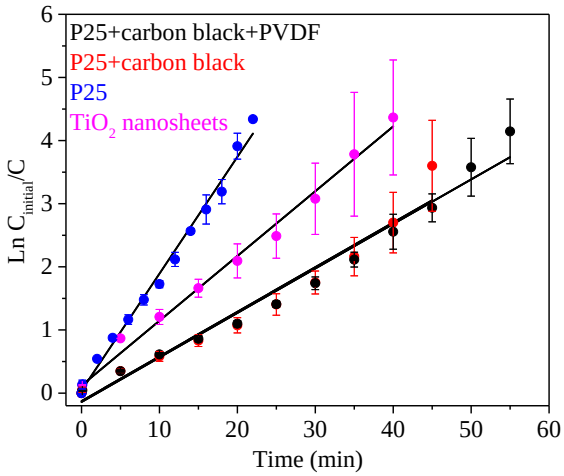

Fig. 30 First order liner transforms of disappearance of MB for photocatalysts (P25, TiO_2 nanosheets, PC and PCP) under UV irradiation

Table 1. Kinetics results and pseudo-first-order fitting ($C_{initial}$: initial MB concentration, k: rate constant, r^2: correlation coefficient)

Photocatalyst	$C_{initial}$	k (min^{-1})	r^2
P25	5 ppm	0.185	0.9912
TiO_2 nanosheets	5 ppm	0.1026	0.992
PC	5 ppm	0.0707	0.957
PCP	5 ppm	0.0705	0.978

CHAPTER 4

FUTURE WORKS

4.1 First approach

LDH can act as semiconductors with specific metal anions inside the material, for instance, ZnCr-LDH, NiFe-LDH, CoAl-LDH, etc. It was turned out that the combination of metals, for instance, Zn/Cr, Mg/Cr, Zn/Fe, Mg/Fe, Cu/Cr, Co/Cr, and Ni/Fe, results in the photoresponse of LDH in visible-light region. We tried MgAl-LDH before since MgAl-LDH is proved to be a good adsorbent for selenium and chromium in our previous studies. We combined MgAl-LDH with TiO_2 for the degradation of selenium and chromium and it wasn't turned out to be quite useful. So we thought it might be a promising approach if we could use other kinds of LDH which can also act as photocatalyst instead. Properties of those LDH materials, such as the large surface area, surface hydroxyl groups and exchangeable interlayer anions make them a very attractive choice in the field of OER, ORR, water splitting and also photodegradation of environmental pollutants.[66] Hwang et al. used layer-by-layer assembly method to prepare ZnCr-LDH nanosheets/TiO_2 nanosheets hybrid material as photocatalyst for O_2 evolution and it turned out to be an efficient visible light active photocatalyst. Ning et al. synthesized TiO_2/graphene/NiFe-LDH nanorod array as photoanodes for photoelectrochemical water splitting. The synergetic effect of the material lead to largely enhanced photoconversion efficiency.[67] Since Co^{2+} and Cr^{3+} anion might have impact on the environments, we thought NiFe-LDH is a good choice to start with. So the next step NiFe-LDH nanosheets/TiO_2 nanosheets hybrid material will be synthesized. We expect

that there will be synergetic effect between NiFe-LDH and TiO_2 and photodegradation efficiency of selenium or chromium will be improved.

4.2 Second approach

As shown both in the SEM image of TiO_2 nanosheets and the photodegradation performance of methylene blue, carbon black and PVDF existing in the TiO_2 nanosheets samples have great impact on both the morphology and photodegradation ability of the TiO_2 nanosheets. The further attempts will mainly focus on how to avoid using carbon black and PVDF during the synthesis of TiO_2 nanosheets. The first attempt could be using chemical lithiation method to exfoliate bulk TiS_2. As shown in literature,[68] n-butyllithium could be added into bulk TiS_2 under Ar atmosphere to directly exfoliate TiS_2. Another attempt could be replacing carbon black with other types of carbon. For instance, graphene/TiO_2 composite has proved to be effective as photocatalysts.[5, 69, 70] Therefore, graphene could be used here to see if it will improve the photocatalytic ability of the TiO_2 nanosheets sample.

REFERENCES

[1] G. Dong and L. Zhang, *The Journal of Physical Chemistry C*, 2013, **117**, 4062-4068.

[2] Q. Cheng, C. Wang, K. Doudrick and C. K. Chan, *Applied Catalysis B: Environmental*, 2015, **176**, 740-748.

[3] C. Mondal, M. Ganguly, J. Pal, A. Roy, J. Jana and T. Pal, *Langmuir*, 2014, **30**, 4157-4164.

[4] J. J. Testa, M. A. Grela and M. I. Litter, *Environmental Science & Technology*, 2004, **38**, 1589-1594.

[5] Y. Zhao, D. Zhao, C. Chen and X. Wang, *Journal of Colloid and Interface Science*, 2013, **405**, 211-217.

[6] J. Burger and M. Gochfeld, *Environmental Research*, 2005, **99**, 403-412.

[7] W. Jin, H. Du, S. Zheng and Y. Zhang, *Electrochimica Acta*, 2016, **191**, 1044-1055.

[8] C. E. Barrera-Díaz, V. Lugo-Lugo and B. Bilyeu, *Journal of Hazardous Materials*, 2012, **223-224**, 1-12.

[9] C. d. G. Sampaio, L. S. Frota, H. S. Magalhães, L. M. U. Dutra, D. C. Queiroz, R. S. Araújo, H. Becker, J. R. R. de Souza, N. M. P. S. Ricardo and M. T. S. Trevisan, *International Journal of Biological Macromolecules*, 2015, **78**, 273-279.

[10] H. Hartikainen, *Journal of Trace Elements in Medicine and Biology*, 2005, **18**, 309-318.

[11] N. Bleiman and Y. G. Mishael, *Journal of Hazardous Materials*, 2010, **183**, 590-595.

[12] N. Takeno, *Geological survey of Japan open file report*. 2005, **419**, 102.

[13] J. Torres, V. Pintos, S. Domínguez, C. Kremer and E. Kremer, *Journal of Solution Chemistry*, 2010, **39**, 1-10.

[14] T. Nishimura, R. Hata and F. Hasegawa, *Molecules*, 2009, **14**, 3567.

[15] Y. Zhang, C. Amrhein and W. T. Frankenberger, *Science of The Total Environment*, 2005, **350**, 1-11.

[16] S. C. B. Myneni, T. K. Tokunaga and G. E. Brown, *Science*, 1997, **278**, 1106-1109.

[17] L. S. Balistrieri and T. T. Chao, *Soil Science Society of America Journal*, 1987, **51**, 1145-1151.

[18] H. Wijnja and C. P. Schulthess, *Journal of Colloid and Interface Science*, 2000, **229**, 286-297.

[19] M. Rovira, J. Giménez, M. Martínez, X. Martínez-Lladó, J. de Pablo, V. Martí and L. Duro, *Journal of Hazardous Materials*, 2008, **150**, 279-284.

[20] A. B. Holmes and F. X. Gu, *Environmental Science: Nano*, 2016, **3**, 982-996.

[21] C. N. R. Rao, J. N. Behera and M. Dan, *Chemical Society Reviews*, 2006, **35**, 375-387.

[22] H. Fu, G. Lu and S. Li, *Journal of Photochemistry and Photobiology A: Chemistry*, 1998, **114**, 81-88.

[23] L. Liu, Y. Yuan, F.-b. Li and C.-h. Feng, *Bioresource Technology*, 2011, **102**, 2468-2473.

[24] C. Garbisu and I. Alkorta, *Bioresource Technology*, 2001, **77**, 229-236.
[25] T. T. Y. Tan, D. Beydoun and R. Amal, *Journal of Molecular Catalysis A: Chemical*, 2003, **202**, 73-85.
[26] T. T. Y. Tan, C. K. Yip, D. Beydoun and R. Amal, *Chemical Engineering Journal*, 2003, **95**, 179-186.
[27] L. Yang, Y. Xiao, S. Liu, Y. Li, Q. Cai, S. Luo and G. Zeng, *Applied Catalysis B: Environmental*, 2010, **94**, 142-149.
[28] L. B. Khalil, W. E. Mourad and M. W. Rophael, *Applied Catalysis B: Environmental*, 1998, **17**, 267-273.
[29] H. Tian, J. Ma, K. Li and J. Li, *Materials Chemistry and Physics*, 2008, **112**, 47-51.
[30] X. Z. Li and F. B. Li, *Environmental Science & Technology*, 2001, **35**, 2381-2387.
[31] S. A. Khayyat, R. Selvin and L. S. Roselin, in *Applied Photosynthesis - New Progress*, ed. M. M. Najafpour, InTech, Rijeka, 2016, DOI: 10.5772/62220, p. Ch. 08.
[32] Z. He, Q. Cai, M. Wu, Y. Shi, H. Fang, L. Li, J. Chen, J. Chen and S. Song, *Industrial & Engineering Chemistry Research*, 2013, **52**, 9556-9565.
[33] A. Ajmal, I. Majeed, R. N. Malik, H. Idriss and M. A. Nadeem, *RSC Advances*, 2014, **4**, 37003-37026.
[34] L. Mohapatra and K. Parida, *Journal of Materials Chemistry A*, 2016, **4**, 10744-10766.
[35] G. Fan, F. Li, D. G. Evans and X. Duan, *Chemical Society Reviews*, 2014, **43**, 7040-7066.
[36] M. Li, L. M. Farmen and C. K. Chan, *Industrial & Engineering Chemistry Research*, 2017, **56**, 2458-2465.
[37] Z. P. Xu, G. S. Stevenson, C.-Q. Lu, G. Q. Lu, P. F. Bartlett and P. P. Gray, *Journal of the American Chemical Society*, 2006, **128**, 36-37.
[38] X. Guo, F. Zhang, S. Xu, D. G. Evans and X. Duan, *Chemical Communications*, 2009, **0**, 6836-6838.
[39] H. G. Yang, C. H. Sun, S. Z. Qiao, J. Zou, G. Liu, S. C. Smith, H. M. Cheng and G. Q. Lu, *Nature*, 2008, **453**, 638.
[40] X. Han, Q. Kuang, M. Jin, Z. Xie and L. Zheng, *Journal of the American Chemical Society*, 2009, **131**, 3152-3153.
[41] H. G. Yang, G. Liu, S. Z. Qiao, C. H. Sun, Y. G. Jin, S. C. Smith, J. Zou, H. M. Cheng and G. Q. Lu, *J. Am. Chem. Soc.*, 2009, **131**, 4078-4083.
[42] P. Wen, H. Itoh, W. Tang and Q. Feng, *Langmuir*, 2007, **23**, 11782-11790.
[43] P. Wen, Y. Ishikawa, H. Itoh and Q. Feng, *The Journal of Physical Chemistry C*, 2009, **113**, 20275-20280.
[44] C. Chen, L. Xu, G. A. Sewvandi, T. Kusunose, Y. Tanaka, S. Nakanishi and Q. Feng, *Crystal Growth & Design*, 2014, **14**, 5801-5811.
[45] H. Yuan, R. Besselink, Z. Liao and J. E. ten Elshof, *Scientific Reports*, 2014, **4**, 4584.
[46] L. Wang and T. Sasaki, *Chemical Reviews*, 2014, **114**, 9455-9486.
[47] J. L. Gunjakar, T. W. Kim, H. N. Kim, I. Y. Kim and S.-J. Hwang, *J. Am. Chem. Soc.*, 2011, **133**, 14998-15007.

[48] Q. Cheng, T. Yang, Y. Li, M. Li and C. K. Chan, *Journal of Materials Chemistry A*, 2016, **4**, 6902-6910.
[49] Q. Cheng, T. Yang, M. Li and C. K. Chan, *Langmuir*, 2017, **33**, 9271-9279.
[50] Z. Zeng, Z. Yin, X. Huang, H. Li, Q. He, G. Lu, F. Boey and H. Zhang, *Angewandte Chemie International Edition*, 2011, **50**, 11093-11097.
[51] Z. Zeng, T. Sun, J. Zhu, X. Huang, Z. Yin, G. Lu, Z. Fan, Q. Yan, H. H. Hng and H. Zhang, *Angewandte Chemie International Edition*, 2012, **51**, 9052-9056.
[52] T. Ohno, M. Akiyoshi, T. Umebayashi, K. Asai, T. Mitsui and M. Matsumura, *Applied Catalysis A: General*, 2004, **265**, 115-121.
[53] W. Ho, J. C. Yu and S. Lee, *Journal of Solid State Chemistry*, 2006, **179**, 1171-1176.
[54] Q. Xiang, J. Yu and M. Jaroniec, *Physical Chemistry Chemical Physics*, 2011, **13**, 4853-4861.
[55] Z. Li, Y. Zhu, F. Pang, H. Liu, X. Gao, W. Ou, J. Liu, X. Wang, X. Cheng and Y. Zhang, *Ceramics International*, 2015, **41**, 10063-10069.
[56] Y.-C. Lin, T.-E. Chien, P.-C. Lai, Y.-H. Chiang, K.-L. Li and J.-L. Lin, *Applied Surface Science*, 2015, **359**, 1-6.
[57] Z. Zeng, C. Tan, X. Huang, S. Bao and H. Zhang, *Energy & Environmental Science*, 2014, **7**, 797-803.
[58] M. S. WHITTINGHAM, *Science*, 1976, **192**, 1126-1127.
[59] E. Long, S. O'Brien, E. A. Lewis, E. Prestat, C. Downing, C. S. Cucinotta, S. Sanvito, S. J. Haigh and V. Nicolosi, *npj 2D Materials and Applications*, 2017, **1**, 22.
[60] W. F. Zhang, Y. L. He, M. S. Zhang, Z. Yin and Q. Chen, *Journal of Physics D: Applied Physics*, 2000, **33**, 912.
[61] R. R. Chianelli, J. C. Scanlon and A. H. Thompson, *Materials Research Bulletin*, 1975, **10**, 1379-1382.
[62] C. J. Howard, T. M. Sabine and F. Dickson, *Acta Crystallographica Section B*, 1991, **47**, 462-468.
[63] M. G. Faba, D. Gonbeau and G. Pfister-Guillouzo, *Journal of Electron Spectroscopy and Related Phenomena*, 1995, **73**, 65-80.
[64] H. Martinez, C. Auriel, D. Gonbeau, M. Loudet and G. Pfister-Guillouzo, *Applied Surface Science*, 1996, **93**, 231-235.
[65] D. Y. Oh, Y. E. Choi, D. H. Kim, Y.-G. Lee, B.-S. Kim, J. Park, H. Sohn and Y. S. Jung, *Journal of Materials Chemistry A*, 2016, **4**, 10329-10335.
[66] S. Nayak, L. Mohapatra and K. Parida, *Journal of Materials Chemistry A*, 2015, **3**, 18622-18635.
[67] F. Ning, M. Shao, S. Xu, Y. Fu, R. Zhang, M. Wei, D. G. Evans and X. Duan, *Energy & Environmental Science*, 2016, **9**, 2633-2643.
[68] U. Gupta, B. G. Rao, U. Maitra, B. E. Prasad and C. N. R. Rao, *Chemistry – An Asian Journal*, 2014, **9**, 1311-1315.
[69] G. Jiang, Z. Lin, C. Chen, L. Zhu, Q. Chang, N. Wang, W. Wei and H. Tang, *Carbon*, 2011, **49**, 2693-2701.
[70] Q. Xiang, J. Yu and M. Jaroniec, *Nanoscale*, 2011, **3**, 3670-3678.